Materials Horizons

ROYAL SOCIETY OF CHEMISTRY

COMMUNICATION

View Article Online
View Journal | View Issue

Cite this: *Mater. Horiz.*, 2026, **13**, 1350

Received 3rd September 2025,
Accepted 24th October 2025

DOI: 10.1039/d5mh01681a

rsc.li/materials-horizons

Strong and flexible graphene oxide paper for humidity responsive origami metamaterials

Yiwen Chen, †[a] Jun Cai,†[b] Alireza Seyedkanani,[b] Abdolhamid Akbarzadeh *[b] and Marta Cerruti [a]

Origami, the art of paper folding, can transform sheets into three-dimensional (3D) configurations and reshape deployed structures into folded forms, inspiring the design of deployable and multifunctional structures. Graphene oxide (GO) flakes can be assembled into papers that are promising substrates to fabricate actuators because of their light weight, high surface area for integration of functional components, and responsiveness to stimuli. In this work, we develop macroscopic deployable GO origamis with anisotropic mechanical properties, structural bistability, and humidity-responsive deformations. To produce strong yet flexible GO papers, we propose a high-throughput fabrication method by drop-casting GO suspensions on a wet cellulose substrate. The cellulose allows retaining water within the GO flakes during evaporation, enhancing the flexibility and toughness of the resulting GO paper. We fabricate GO Miura-ori and Kresling origamis that unfold in humid environments and fold upon water evaporation, thanks to the hygroscopic expansion of GO combined with the 3D origami design. This enables the creation of programmable, multifunctional structures that serve as actuators in a two-digit humidity signaling device. The deployable GO origamis, powered by origami engineering and the humidity responsiveness of graphene materials, offer new opportunities for the design of next-generation graphene metamaterials and responsive soft robots.

New concepts

We achieve for the first time programmable humidity responsiveness in graphene oxide (GO) metamaterials by integrating 3D origami design with facile fabrication of large-scale GO membranes. The breakthrough lies in producing flexible yet strong GO papers by retaining water within the structure, and exploiting the intrinsic hygroscopic expansion of GO nanosheets to enable large-scale motion of origami-inspired architectures. Rather than relying on composition gradients and asymmetric expansion to induce bending and twisting as done in previous works, we employ origami crease topological design to achieve multidirectional motions, multiple actuation modes, and device-level state indication/memory functions in humidity-responsive GO metamaterials, demonstrating that mesoscale geometric constraints can dictate macroscopic motions. This work not only expands responsive graphene-based systems, but also offers new insights into environmentally responsive actuators that emerge from the interplay between material chemistry and structural geometry. It provides a generalizable strategy for creating scalable, energy-free actuators and adaptive materials, with implications for soft robotics and deployable multifunctional devices.

Introduction

Since the discovery of graphene in 2004,[1,2] many researchers have developed methods to harness its extraordinary properties for developing advanced materials at both micro- and macroscopic scales. The oxidized form of graphene known as graphene oxide (GO) has attracted considerable interest due to its solubility in water, making it a promising candidate for large-scale fabrication of graphene-based materials in diverse forms, *e.g.*, colloids, paper sheets, or porous monoliths.[3–7] GO's abundant oxygen-containing groups, such as carboxyl and hydroxyl, provide reaction sites for post-functionalization, and are sensitive to changes in pH, ionic strength, and temperature, therefore providing opportunities to impart additional functionalities to the resulting materials.[8]

New forms of GO-based topological materials can draw inspiration from the recent advances in mechanical metamaterials.[9–11] By tailoring the mechanical properties and programming the spatial distribution of topological modular units, metamaterials can achieve remarkable behavior beyond what is offered by the constitutive building blocks.[12] Deployable origamis, formed based on the traditional art of paper folding, are a class of mechanical metamaterials that possesses shape-morphing and locomotion capabilities, reconfigurability, mechanical tunability and metastability.[13–19] Responsive materials can be used to form origami-based actuators and devices stimulated by changes in

[a] *Department of Mining and Materials Engineering, McGill University, Montreal, QC H3A 0C5, Canada. E-mail: marta.cerruti@mcgill.ca*
[b] *Department of Bioresource Engineering, McGill University, Montreal, QC H9X 3V9, Canada. E-mail: hamid.akbarzadeh@mcgill.ca*
† Equal contribution.

temperature,[20] magnetic field,[21] pH,[22,23] light[24] and pressure[25] in the surrounding environment.

Current research has shown some examples of deployable graphene and GO structures, such as autonomous pyramids,[23] self-assembled polyhedrons,[26] and self-opening flowers[27,28] driven by hydrogen bonding, capillary forces, and electrostatic interactions. However, the size of these stimuli-responsive structures has not exceeded 2 cm. A few studies produced GO origami cranes and Miura-ori pattern at decimeter scale,[29–31] however, responsive graphene- or GO-based complex origami designs remain unexplored.

Most studies on deployable GO-composite structures have exploited the humidity responsiveness of GO to create simple bilayer or multilayer ribbons,[32–34] which are then used to construct shapes such as hands,[35–37] legs,[38] and boxes.[39] In these studies, motion is achieved through asymmetric expansion of the GO ribbons, either due to the presence of humidity gradients in the surrounding environment[40,41] or because of the hygroscopic expansion coefficient gradients within the ribbon.[42,43] The first approach presents practical challenges, because it is difficult to precisely maintain a stable humidity gradient, and even harder to create dynamic humidity changes in the environment to trigger complex motions. The second approach requires hygroscopic expansion coefficient mismatch within bilayer or multilayer films, such as local patterning or gradient engineering of composition, thickness, GO reduction degree, or crystal orientation.[42–45] This is not straightforward to achieve and hinders efficient production of macroscopic actuators. The motions achievable through ribbon bending are also limited. Even though ''programmable'' humidity responsiveness in GO-based actuators was reported through this approach, the motions refer to predefined, simple and continuous motions, including bending/unbending, twisting/straightening, opening/closing, and walking or crawling.[44,45] Linear movements, multi-directional motions, and bi-/multistable deformation are yet to be realized in GO actuators; deployable, programmable, and multifunctional GO origami also remain unexplored.

GO paper with adequate flexibility is required to produce deployable GO origamis and to ensure that the hinges remain intact upon bending. The first reported GO Miura-ori was recently produced using GO paper with a tensile failure strain of $\sim$10%, which contributed to the flexibility of GO papers upon bending into origamis.[29] The flexibility was improved by soaking the GO paper in ethanol; the ethanol molecules were intercalated within the GO layers and acted as plasticizers, decreasing brittleness.[29] However, the ultimate tensile strength (UTS) was significantly reduced due to the lack of intermolecular interactions between flakes. In addition, the introduction of ethanol may affect humidity responsiveness.

Water retained between GO flakes has also been shown to act as plasticizer and improve the flexibility of GO paper; intercalated water improves GO paper strength thanks to hydrogen bonding and helps preventing fracture during deformation.[46] However, a direct relationship between water content and GO paper mechanical properties has yet to be established.

In this study, we introduce a scalable method to fabricate flexible yet strong GO paper that can be used to create first decimeter-scale GO origami metamaterials with topology-programmed humidity-driven actuation. Unlike the commonly used vacuum-filtration or wet-spinning methods, which are slower and size-constrained, our approach produces multiple sheets of different dimensions by evaporating GO suspensions in molds placed on cellulose-paper substrates. We show that water content in the GO paper, increased by evaporating GO on wet cellulose substrates, enhances flexibility of the GO paper and allows achieving multiple kinematic modes in GO origamis, beyond conventional bending and twisting. By integrating humidity responsiveness of GO and mono-/bi-stable origami design, we develop a humidity-responsive signalling device. These unprecedented achievements open opportunities for next-generation responsive graphene oxide metamaterials and autonomous soft robots.

Results and discussion

Strong and flexible GO paper

We first aim to determine a fabrication method to produce flexible and strong GO papers. Previous studies used mainly two methods to prepare GO paper: evaporation, where a GO suspension is simply allowed to dry on a substrate, or filtration, where assembly is driven by filtering a GO suspension through a filter.[47] We summarize in Fig. S1 and Table S1 the key mechanical properties, *i.e.*, failure strain and compliance, of GO papers prepared through either evaporation (GO/E) or filtration (GO/F) thus far.[46–66] GO-reinforced polymer composite papers are excluded in this summary, as the mechanical properties are highly affected by their polymeric components.

GO papers with higher tensile failure strain can endure greater elongation before fracture upon bending, as the upper GO layers are essentially under tensile stress. Compliance, the inverse of stiffness, indicates the ability of GO layers to deform elastically under a tensile force; thus, higher compliance contributes to better flexibility of the bended region. GO/E papers exhibit higher failure strain and compliance compared to GO/F papers. This may be explained by the looser arrangement of GO flakes in GO/E papers, resulting in a wrinkled structure that can act like a spring and is stretched before eventual fracture.[47,48] Another reason that could explain these differences is water content.[46] Water is removed from the GO suspension through capillary forces during the evaporation process of making GO papers, while vacuum forces remove the water during filtration (Fig. S2a);[5,67] this may imply a higher water content in GO/E than GO/F paper, although to the best of our knowledge, no one has yet studied this correlation.

Based on this hypothesis, to achieve GO paper with high failure strain and compliance, we prepare GO/E papers through evaporation in the presence of a water reservoir, which can continuously supply moisture to the GO paper during evaporation (Fig. S2b). We first crosslink GO flakes with calcium chloride ($CaCl_2$) and then drop cast the suspension onto a

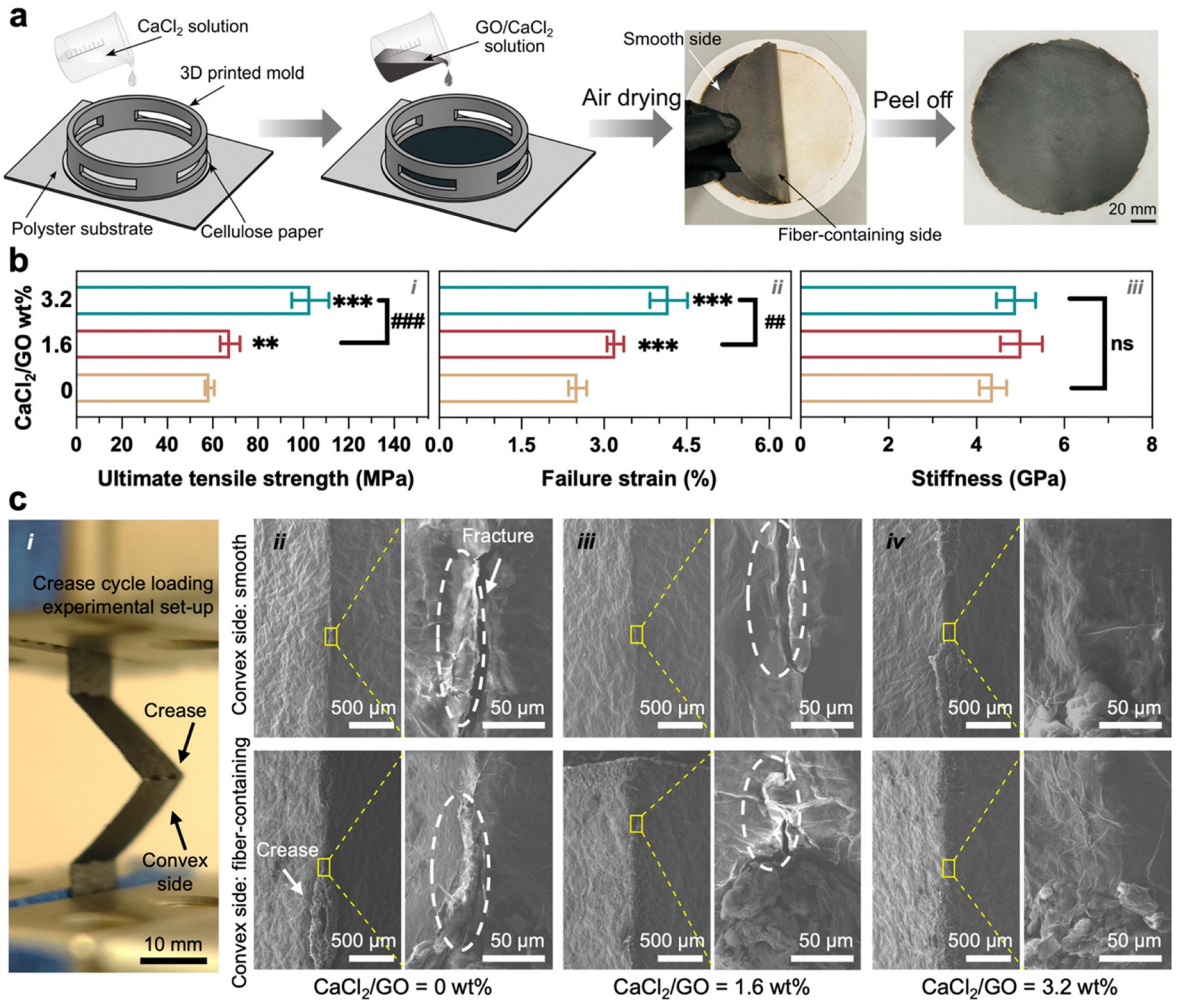

Fig. 1 (a) Schematic drawing showing the GO@C/E paper fabrication process. (b) UTS (i), failure strain (ii), and stiffness (iii) of GO@C/E containing different weight percentages of $CaCl_2$ (n = 4 independent samples). The data are represented as the mean ± standard deviation. The * and # signs indicate statistically significant differences between GO papers with different $CaCl_2$ crosslinking degree; *: between 0 wt% and 1.6 or 3.2 wt%, and #: between 1.6 wt% and 3.2 wt%. Differences are calculated by Student's t-test (** or ## $P < 0.01$, ### or *** $P < 0.001$). (c) Bending and release tests on creased GO papers. (i) Experimental set-up. The samples are folded at the crease, and the convex side of the samples can be either smooth or fiber-containing. ((ii) and (iv)) SEM images of the convex sides of GO papers (top row: smooth; bottom row: fiber-containing) after 60 bending and release cycles. The GO papers contain 0 (ii), 1.6 (iii) and 3.2 (iv) wt% of $CaCl_2$. The fractures are highlighted by the dashed circles.

cellulose paper wetted with $CaCl_2$ solution, which is placed on a flat polyester substrate (Fig. 1a). The concentration of Ca^{2+} ions is the same in the GO/$CaCl_2$ suspension and in the cellulose paper to avoid the dilution of Ca^{2+} within the GO paper. The Ca^{2+} ions are introduced to ionically crosslink the GO flakes, increasing the fracture resistance during deformation.[52] After drying in air at a relative humidity (RH) 54% for four days, a self-standing GO paper can be peeled off the cellulose filter (Fig. 1a). We refer to this paper as GO@C/E in the following discussion, where C stands for cellulose.

Scanning electron microscope (SEM) shows the layered cross section of GO@C/E (Fig. S3). The top surface facing air is smooth, while the bottom side contacting the cellulose paper has residues of cellulose fiber (Fig. 1a and Fig. S3). We evaluate the effect of $CaCl_2$ content varying between 0 and 3.2 wt% on the mechanical properties of GO@C/E. Higher $CaCl_2$ contents result in the gelation of GO, which impedes casting the suspensions. As the $CaCl_2$ wt% increases, the ultimate tensile strength (UTS) and failure strain are significantly enhanced, while the stiffness does not change significantly (Fig. 1b).

We then introduce a crease in GO@C/E paper strips through laser cutting (see SI, Section S2.3) and investigate the microstructure of the GO@C/E paper close to the crease before and after 30 and 60 cycles of bending and release (Fig. 1c-(i) and Fig. S4, S5). SEM images show the presence of fractures in the un-crosslinked (*i.e.*, 0 wt% of $CaCl_2$) GO@C/E sample if the strip is bent so that the convex side is smooth, even before the bending and release cycle (Fig. S4). This can be explained by the lower tensile strength and failure strain of this paper, which allows crack formation due to stress concentration at the crease and its propagation on the smooth side during the initial folding. Conversely, the fiber-containing side remains intact; this could be due to bridging of GO flakes by the fibers (Fig. S4).

After 30 cycles, fractures appear on both fiber-containing and smooth sides of un-crosslinked samples, and on the smooth side of samples crosslinked with 1.6 wt% of $CaCl_2$ (Fig. S5). After 60 cycles, samples crosslinked with 3.2 wt% of $CaCl_2$ are the only ones that do not show fracture on either side (Fig. 1c). This result indicates the crucial role of crosslinking in preventing the formation and propagation of cracks upon bending; differences observed at lower $CaCl_2$ wt% between the smooth and the fiber-containing sample sides also prove the importance of the presence of cellulose fibers in enhancing the structural integrity of GO paper.

Upon bending towards either the fiber-containing or the smooth side, the radii of curvature of uncreased GO@C/E papers crosslinked with 3.2 wt% $CaCl_2$ are below 500 μm (Fig. S6). This is significantly lower than GO/F papers with similar thickness reported in a previous study,[46] where the smallest radius of curvature was ~1000 μm.

To confirm whether the water content plays a role in increasing compliance and failure strain, we compare the mechanical properties and water content of GO@C/E and other GO papers prepared by evaporation and filtration onto different substrates, using GO crosslinked by 3.2 wt% of $CaCl_2$ and keeping the same amount of GO per unit of surface area. Papers prepared by filtration through polycarbonate (PC) membranes are called GO@PC/F, while those prepared by evaporation over PC membranes and polyester (PET) plastic sheets are named GO@PC/E and GO@PET/E, respectively. All samples prepared by evaporation are dried in the same conditions as GO@C/E, while the GO@PC/F is prepared using a glass filter kit to which vacuum is applied for three days. To decouple the effect of presence of cellulose fibers and water content on the mechanical properties of GO@C/E, we also prepare a set of samples with the same method as that used for GO@C/E, but we remove the cellulose fibers by wiping the side of the paper in contact with the cellulose membrane with ethanol (see SI, Section S2.2). This was sufficient to remove the cellulose fibers, as confirmed by both Fourier-transform infrared spectroscopy (FTIR) and SEM (Fig. S7). We refer to this group as GO@C/E-wiped.

GO papers fabricated with different methods all show a layered cross-section (Fig. 2a); as expected,[46,47,49,54] GO papers prepared by evaporation have a more loosely packed, wrinkled microstructure with interlayer gaps and higher thickness (Table S2) than those prepared by filtration. Tensile tests (Fig. 2b and Fig. S8) show a lower failure strain for the GO@C/E-wiped compared to GO@C/E, supporting the aforementioned finding that the cellulose fibers help decrease fracture at the edge of the creases. Among all produced GO papers, GO@PC/F shows the lowest elongation and toughness, and the highest stiffness. This aligns with prior studies that showed lower failure strain and compliance for membranes prepared by filtration compared to evaporation (Fig. S1).[5,46–64,66,68]

Both GO@C/E and GO@C/E-wiped show significantly higher failure strain, lower stiffness, and higher toughness than all other GO papers (Fig. 2b). Since there are no differences in membrane structure and composition among GO@C/E-wiped, GO@PC/E and GO@PET/E, we perform thermogravimetric analysis (TGA) to evaluate whether water content may be responsible for the tensile test differences. Fig. 2c plots the

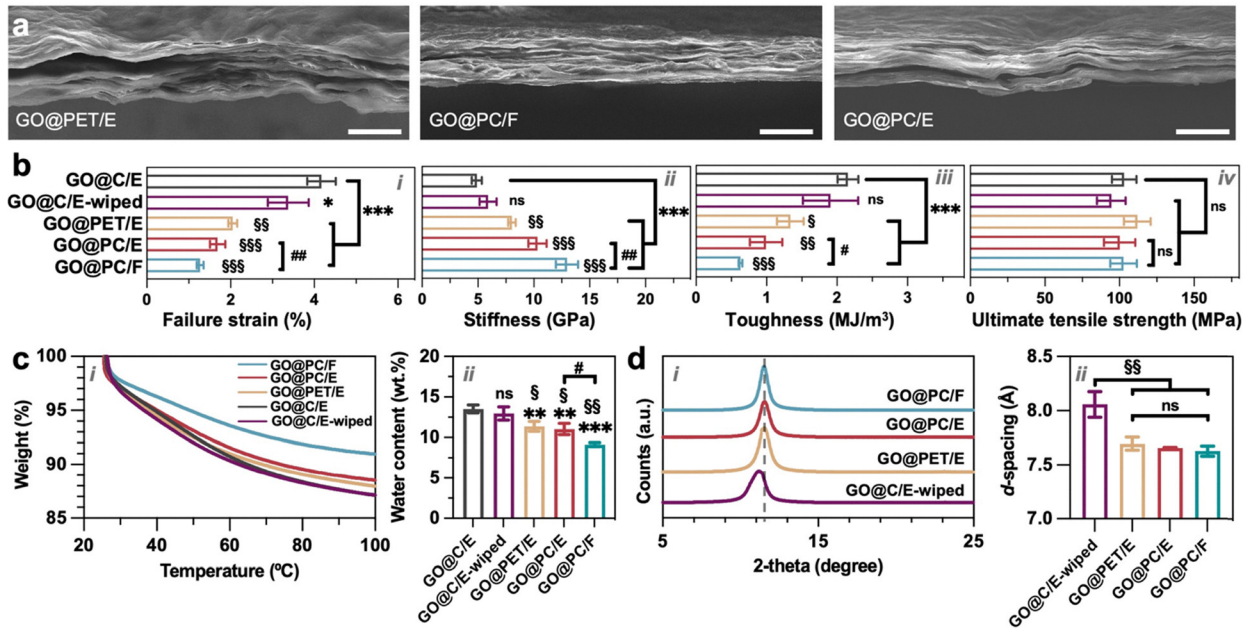

Fig. 2 (a) SEM cross-section images of GO@PET/E, GO@PC/F, and GO@PC/E papers. Scale bar = 20 μm in all images. (b) Tensile failure strain, stiffness, toughness and UTS of GO papers (n = 4). (c) TGA curves recorded in air (i), and weight loss between room temperature and 100 °C, corresponding to water content (ii) (n = 3). (d) XRD spectra (i) and d-spacing (ii) (n = 3). The data are represented as the mean ± standard deviation. The *, # and § signs indicate statistically significant differences, *: between different samples and GO@C/E; #: between GO@PC/F and GO@PC/E; §: between different samples and GO@C/E-wiped. Differences were calculated by Student's t-test (*, # or §P <0.05, **, ## or §§ P <0.01, ***, ### or §§§P <0.001).

weight loss measured up to 100 °C, which corresponds to the water content. All the evaporated GO papers have a higher water content than the ones prepared by filtration and GO@C/E and GO@C/E-wiped papers have the highest water content. The presence of less water in the filtered membranes indicates that the vacuum forces can eliminate more water than simple evaporation. To explain the larger water content in GO@C/E and GO@C/E-wiped compared to other evaporated membranes, we hypothesize that as the GO suspension becomes more concentrated upon drying, water in the cellulose filter paper moves from cellulose to GO and is trapped within the GO flakes. The correlation between water content and failure strain and toughness shown by Fig. 2b and c confirm our initial hypothesis, and may be explained by the formation of hydrogen bonds between water and the oxygen-containing groups of GO, acting as ''soft'' connections between flakes when GO paper is subjected to a stress condition; this dissipates energy and allows layers to slide on each other, thus preventing crack propagation.

X-ray diffraction (XRD) results provide additional evidence of higher water content in GO papers prepared over wet cellulose paper. Previous studies have shown that a larger water content results in a higher interlayer spacing (commonly termed as *d*-spacing) of GO membranes.[69,70] To exclude the interference of cellulose, we compare the *d*-spacings of GO@C/E-wiped, GO@PET/E, GO@PC/F and GO@PC/E. All GO papers show the characteristic peak at 2-theta around 11°–12° (Fig. 2d), corresponding to diffraction caused by the stacked GO layers.[71] The *d*-spacing of GO@C/E-wiped is significantly higher than that of all other samples, which further confirms the presence of more intercalated water molecules. This change is not associated with the process of wiping the paper with ethanol, as shown in a control experiment where we wipe with ethanol GO@PET/E paper and obtain the same *d*-spacing as before wiping (Fig. S9). The increase in *d*-spacing of GO papers as the water content increases is confirmed through molecular dynamics (MD) simulation (Fig. S10, see SI, Section S3.4 for more details).

These results overall show that the presence of a cellulose membrane as a substrate for GO evaporation not only reinforces the final GO paper through residual cellulose fibers but also promotes water intercalation to strengthen interlayer interactions during evaporation. Both effects are crucial to create strong and flexible GO paper suitable for origami fabrication.

GO origami

After proving the excellent compliance and resistance to fracture upon bending of GO@C/E, we proceed to use this GO paper to make GO-based origamis. We first compare GO@C/E with two commonly used papers for making origamis, *i.e.*, a standard printer paper and an origami paper (Fig. S11). GO@C/E paper shows a comparable fracture strain to standard printer paper, but significantly higher UTS, stiffness and toughness than both standard printer and origami papers (Fig. S11d). The higher stiffness of GO@C/E paper enables GO-based origami structures to retain their 3D architecture, despite being significantly thinner than origami made from standard printer and origami papers (Fig. S11).

We adopt a basic origami pattern, *i.e.*, Miura-ori, and then fabricate different Miura-ori-based architected metamaterials. A standard Miura-ori origami pattern consists of repeated parallelograms defined by two vectors of lengths a and b and the angle between them θ (Fig. 3a).[72,73] In this study, we use a cell with $a = b = 15$ mm and $\theta = 60°$ as the constitutive unit cell to prepare all Miura-ori-based origami architectures. Leveraging various combinations of Miura-ori units in different arrangements, *i.e.*, aligned, zigzag, edge, and crossed assemblies, we fabricate four distinctive Miura-ori-based GO-based metamaterials.

We create Miura-ori tubes by assembling two mirrored Miura-ori strips with double-sided tape, enabling foldability in two directions (Fig. 3b).[74] Examples of the Miura-ori and Miura-ori tubes made of GO@C/E paper are shown in Fig. 3c, confirming the flexibility of the GO@C/E paper for producing origami architectures. We connect multiple Miura-ori tubes in different arrangements to create Miura-ori-based metamaterials (Fig. 3d–g). In the aligned coupling assembly, two identical Miura-ori tubes are connected by taping the side surfaces of two parallel tubes to each other (Fig. 3(d1) and (d2)).[73] In the zipper coupling assembly, one Miura-ori tube is rotated before gluing its side surface to another one (Fig. 3(e1) and (e2)).[73] Beyond these two standard configurations, we explore two other configurations: edge coupling, which involves connecting two parallel Miura-ori tubes solely by one edge and without full surface adhesion (Fig. 3(f1) and (f2)); and crossed coupling, which entails positioning two Miura-ori tubes perpendicular to each other, forming a cross-like structure and then taping adjacent surfaces (Fig. 3(g2) and (g3)). These units are then tessellated in space, achieving different Miura-ori-based GO-based metamaterials (Fig. 3(d3)–(g3)). The resulting GO@C/E Miura-ori metamaterials are shown in Fig. 3(d4)–(g4).

Fig. 4a shows the stress–strain curves for the four fabricated GO@C/E Miura-ori architected metamaterials in different directions recorded after several uniaxial load–unload cycles, implemented by applying a compressive displacement of 10 mm; this is performed to ensure a stable response in the origami materials and to mitigate the risk of overestimating their mechanical properties. All GO@C/E architected metamaterials exhibit anisotropic mechanical properties under compression. The aligned assembly demonstrates foldability in all directions, with the *z*-direction (*i.e.*, the longitudinal direction of Miura-ori tube) exhibiting a higher load-bearing capacity. In contrast, the other three GO@C/E architected metamaterials can only be folded in the *x*- and *z*-directions, remaining locked and rigid in *y*-direction. Pictures showing examples of folding along *x*- and *z*-directions and rigidity along the *y*-direction for the zipper assembly are shown in Fig. 4b; further details regarding deformation of other GO@C/E architected metamaterials can be found in the SI, Fig. S12–S14. In directions where the structures can be folded, the stress–strain response is characterized by three distinct regions:[75,76] (i) an initial linear elastic response due to the recoverable folding of the creases; (ii) a departure from linearity to a plateau stress caused by bending of the panels and the plastic deformation around

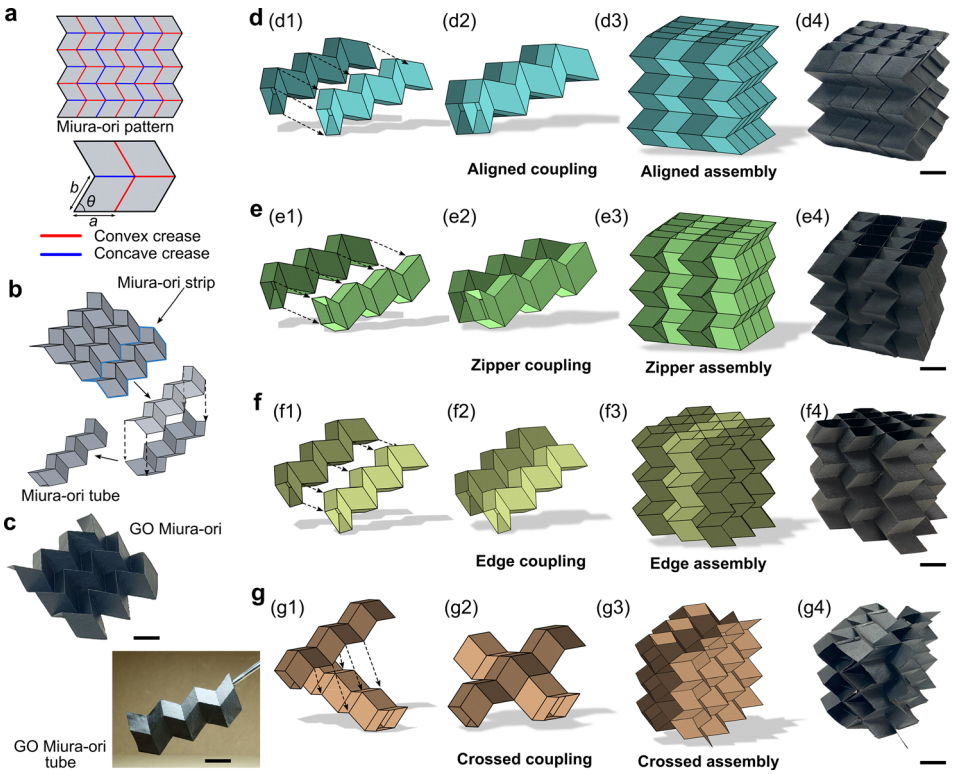

Fig. 3 Assembly of GO Miura-ori metamaterials. (a) Schematic illustration of the Miura-ori pattern and Miura-ori unit cell characterized by $a = b = 15$ mm and $\theta = 60°$. (b) Formation of Miura-ori tube by assembling two mirror Miura-ori strips. (c) Digital photographs of GO@C/E Miura-ori and Miura-ori tube. 3D Miura-ori architected metamaterials based on different coupling configurations of Miura-ori tubes: (d) aligned assembly, (e) zipper assembly, (f) edge assembly, and (g) crossed assembly. While subpanels (1–3) are schematic illustrations of the process, subpanels (4) showcase Miura-ori architected metamaterials fabricated of GO@C/E paper. Scale bars: 15 mm.

creases; and (iii) final stiffening due to the contact between the panels. The stiffness of the GO@C/E architected metamaterials in *x*-, *y*- and *z*-directions calculated as the slope of the stress–strain curve in the initial elastic region is presented in Fig. 4c. The highest stiffness is found for the crossed assembly in the *y*-direction; this is due to its complete lack of foldability in this direction (Fig. S14), leading to an abrupt increase in stress upon application of a compressive strain.

To evaluate the mechanical stability of the GO@C/E architected metamaterials, we conduct cyclic compressive load–unload tests in the *z*-direction (Fig. 4d and Fig. S15; maximum compressive displacement of 10 mm). The hysteretic behavior is primarily attributed to the plastic deformation of the creases, which also accounts for the cyclic softening.[21,77] The mechanical response of the GO@C/E architected metamaterials stabilizes over the course of the loading–unloading cycles, proving the structural integrity of the origami architectures.

In addition to the Miura-ori based origami structures, GO@C/E paper can also be used to construct origami structures that allow more complex deformations such as rotation during contraction/expansion. An example is the Kresling origami; by selecting appropriate geometrical parameters,[78] Kresling origami can be either monostable or bistable (Fig. 4e). Bistable Kresling possesses a deployed state (B-i in Fig. 4f) and a folded one (B-iv in Fig. 4f), while a monostable Kresling only has a deployed state (M-i and M-iv in Fig. 4f).

Fig. 4f shows the force–displacement responses of the GO@C/E Kresling origami structures under loading and unloading, along with the corresponding pictures at specific deformations. The rotation of the structures under uniaxial compression is clearly observable in the pictures. As expected, when the samples are unloaded, the bistable GO@C/E Kresling remains in the folded state (B-iv in Fig. 4f) when the force decreases to 0 N (displacement around 11 mm), while the monostable GO@C/E Kresling returns to its initial state (M-iv in Fig. 4f). Cyclic compressive load–unload tests conducted on the GO@C/E Kresling origamis prove their excellent structural integrity and stable functionality (*i.e.*, bistability) after cyclic deformations (Fig. S16).

Multifunctional humidity responsive GO origamis

As discussed above, water intercalation in the GO paper can increase the *d*-spacing between GO flakes and enhance the paper flexibility. The many oxygen-containing groups (hydroxyl, carboxyl, and epoxy) on GO flakes form hydrogen bonds with water molecules.[79] Therefore, at higher humidity, water molecules permeate the paper and intercalate between the GO layers, increasing the interlayer spacing (*d*-spacing) and leading to anisotropic swelling of the GO paper. Once the humidity decreases, desorption of water leads to the deswelling of the paper.[69,80] These characteristics can be capitalized to develop humidity-responsive GO origami actuators.

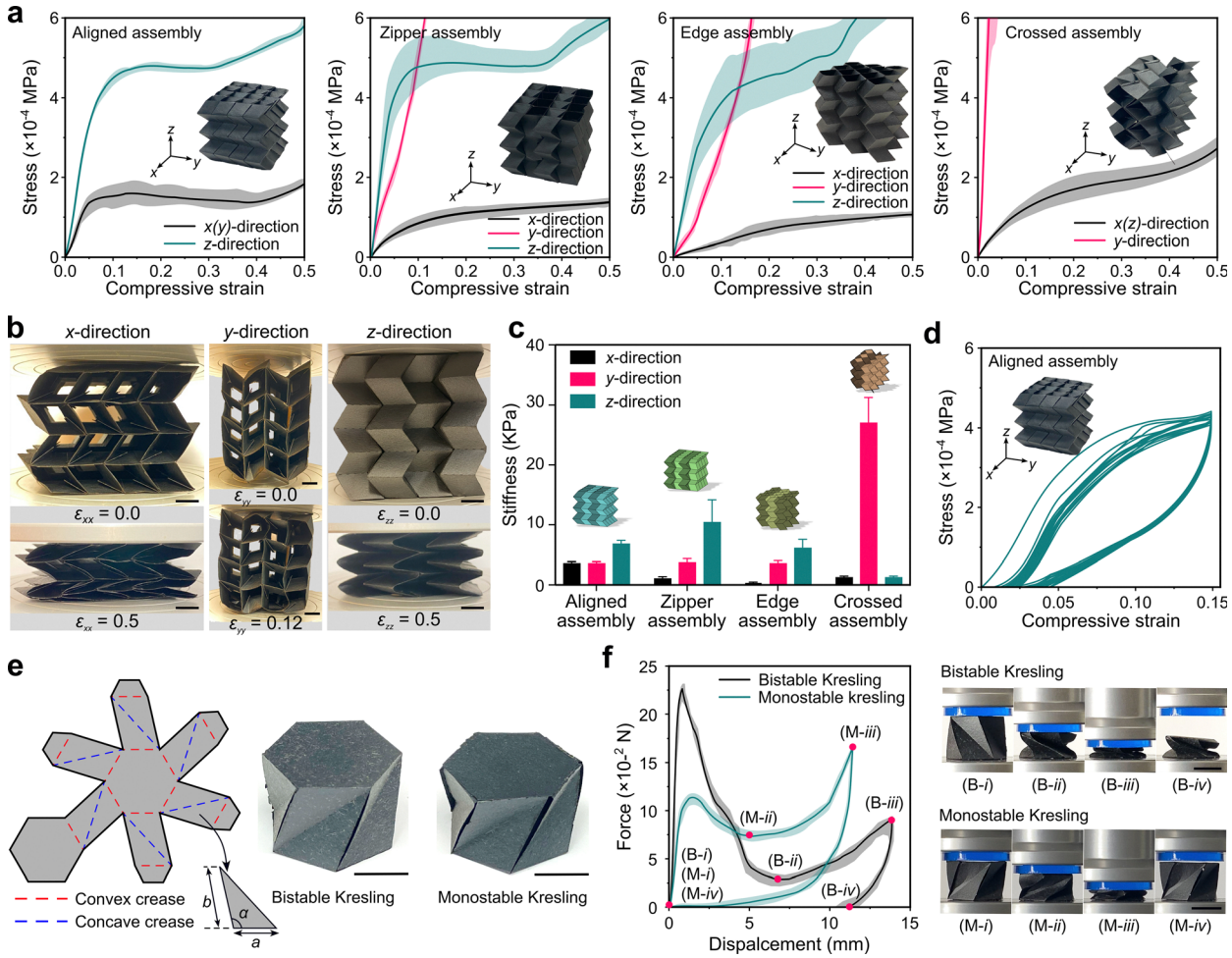

Fig. 4 Mechanical characterization of GO@C/E architected metamaterials. (a) Compressive stress–strain curves of GO Miura-ori architected metamaterials compressed along *x*-, *y*-, and *z*-directions. (b) Digital pictures showing GO@C/E zipper-assembled metamaterials under different compressive strains in *x*-, *y*-, and *z*-directions. The origami can be fully folded in the *x*- and *z*-directions but remains stiff in the *y*-direction. (c) Compressive stiffness of GO@C/E Miura-ori architected metamaterials in different directions. (d) Cyclic (compressive load–unload) responses of aligned assembly; the maximum compressive displacement was 10 mm. (e) Schematic illustration of the Kresling pattern characterized by *a*, *b*, and α along with digital pictures of fabricated samples showing the bistable (a = 13 mm, b = 19.08 mm, and α = 102.77°) and monostable (a = 13 mm, b = 17.77 mm, and α = 106.89°) GO@C/E Kresling origamis. Scale bars: 10 mm. (f) Force–displacement response of bistable and monostable GO@C/E Kresling origamis and digital pictures showing GO@C/E Kresling structures under different compressive displacements. A blue plastic sheet is attached to the surface of the load cell to reduce the friction between the top panel of the GO Kresling and surface of the load cell, enabling its rotation when compressed. B and M denote bistable and monostable designs, respectively. Cyclic (compressive load–unload) responses of Fig. S16(a) bistable GO Kresling and Fig. S16(b) monostable GO Kresling origamis.

We first explore the unfolding of the fabricated GO Miura-ori when relative humidity increases (Fig. 5a). With a change in RH from 34% to 76%, the GO Miura-ori progressively expands to 191% of its original length in the *x*-direction and 117% of its width in the *y*-direction (Fig. 5b and Video S1, SI). Different hygroscopic expansions in the *x*- and *y*-directions are due to the distinctive kinematic relationships between the geometrical features and folding of the Miura-ori.[77,81–83] As the RH reduces from 76% to 35%, the GO Miura-ori gradually folds back to its original dimensions (SI, Video S1).

The mechanism of shape morphing in our GO-based structures differs fundamentally from that of bilayer GO-based films, where shape changes occur due to the different hygroscopic expansion coefficients of the two layers.[42,43] In our developed GO-based material, the shape morphing is made possible by structural designs inspired by origami engineering, and the crucial role that hinges have in this process. At the origami hinges, the GO flakes experience tensile stress on the convex side and compressive stress on the concave side. When the RH increases, the compressed GO flakes expand due to the intercalation of water molecules, resulting in an angle increase at the concave side. At the same time, the absorbed water molecules act as plasticizers, reducing stiffness and tensile stress on the GO at the hinges on the convex side,[29] leading to a decrease in angle at the convex side. As water evaporates, the GO layers at the concave side shrink, and the stiffness increase at the creases, allowing the GO Miura-ori to restore to its pre-deformed folded state. From a thermodynamic perspective,

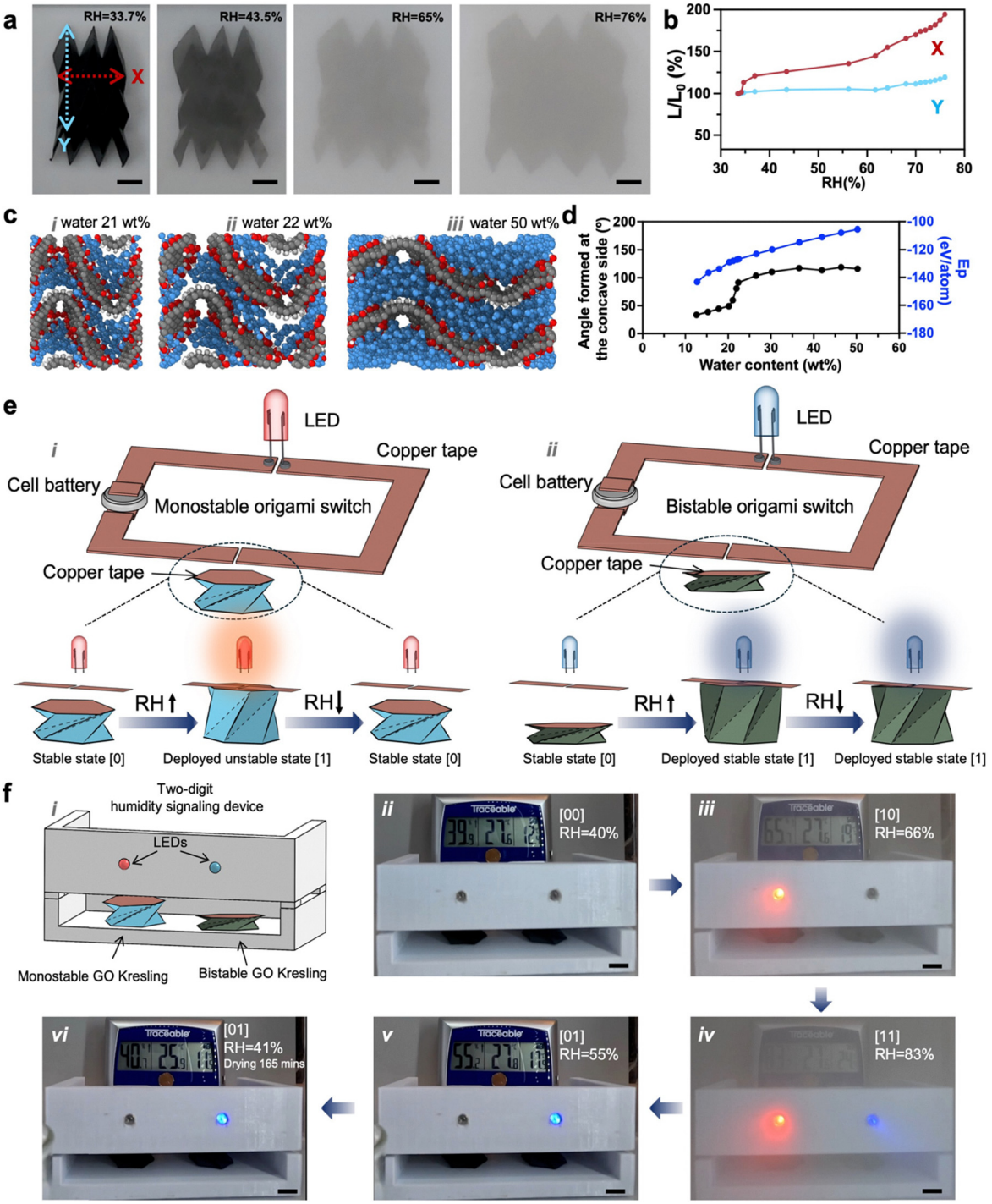

Fig. 5 (a) Pictures showing the unfolding of GO Miura-ori in air at room temperature, with increasing RH, a function of RH increment and at room temperature. The increased opacity is due to the water mist introduced between the camera and the Miura-ori structure. Scale bar =10 mm. (b) Changes in the ratio between the length (L) measured in X- (red) or Y- (blue) directions and the corresponding original length (L_0) (before introducing water mist) as a function of RH (%). (c) MD simulation for the unfolding of GO flakes with creases created by hydrogenation upon increasing water content in the environment. Grey, red, and white atoms represent carbon, oxygen, and hydrogen atoms belonging to the hydrogenated GO. The water molecules are represented in blue. (d) Angle formed at the concave side of bent GO flakes (black) and equilibrium potential energy (E_p, blue) as a function of water content obtained through the MD simulation. (e) Two-digit origami humidity signaling device: schematic showing the electric circuits that contain a switch operated by a monostable (i) or a bistable (ii) Kresling GO origami. Corresponding illustrations of the switch positions and light status when operated by a monostable (left) or bistable (right) Kresling origami as a function of humidity. (f) and (i) Schematic illustration of the two-digit origami humidity signaling device and digital photos of the device at increasing ((ii)–(iv)) and decreasing ((v)–(vi)) RH. Scale bar = 10 mm. The accuracy of the humidity meter is ± 3 RH%; therefore, the last digit showed in the humidity meter is not reported.

this process can be described as follows: strain energy is stored in the folded structure during plastic deformation, which is released as water infiltrates at higher RH. Upon drying, surface tension restores the strain energy and causes the folding of GO flakes according to the laser-cut creases.

These results show that the unfolding of GO flakes upon hydration, previously observed only at the microscopic scale,[84] also applies to GO origamis at the macroscopic scale. This phenomenon is further supported by our models conducted through MD simulation (Fig. 5c and d). In these models, we create creases in the GO layers by surface functionalization with hydrogen atoms (see SI 3.4. and Fig. S17).[81,82,85–87] If fewer water molecules are introduced in the model to mimic lower RH conditions (*e.g.* 21 wt%, Fig. 5c-(i)), the relaxed configuration shows the lowest folding angle at the concave side and the atomic equilibrium potential energy (E_p); this prevents the structure from going back to an unfolded state (Fig. 5c-(i) and d). As more water molecules are introduced in the model, the relaxed stable configuration shows a gradual increase of the folding angle, and a consequent increased atomic E_p (Fig. 5c-(ii), (iii) and d).

We exploit the folding and unfolding of the GO origamis in response to RH to develop a multifunctional, two-digit humidity signaling device (Fig. 5e and f). The device has two separate circuits, each of them including an LED powered by a cell battery; the batteries and the LEDs are connected by copper tape, but the circuits are interrupted by openings (Fig. 5e-(i) and (ii)). One monostable GO Kresling origami (Fig. 5e-(i)) and one bistable GO Kresling origami (Fig. 5e-(ii)), whose top surfaces are covered by copper tape, are placed below the opening of each circuit. At the beginning of the experiment when RH = 40%, both origamis are folded and the LEDs are both off (state [00], Fig. 5f-(ii) and Video S2, SI). When RH increases to 66%, the monostable Kresling gradually unfolds, turning on the red LED (state [10], Fig. 5f-(iii)). More humidity is necessary to deform the bistable Kresling (Fig. S18), consistent with the results discussed regarding force–displacement curves (Fig. 4f). At RH = 83%, the bistable Kresling snaps from the folded state to the deployed state, turning also the blue LED on ([11] state, Fig. 5f-(iv)). As RH decreases to 55%, the monostable GO Kresling gradually folds back to reach its initial state, while the bistable Kresling stays in its deployed stable state (state [01], Fig. 5f-(v)). During drying, hinge stiffness increases at the creases and raises the reverse snap-through threshold; without external compression/torsion, the unit does not fold back. The device remains in this state (*i.e.*, [01]) even after drying for 165 minutes and reaching a RH value comparable to the initial one (Fig. 5f-(vi) and Video S2, SI). The red LED operated by the monostable Kresling is an instant indicator of the environmental RH increase, while the blue LED retains the memory of high environmental humidity. We don't observe obvious differences in origami geometry before and after humidity change. As shown in the cyclic compressive load–unload test of GO Kresling origamis (Fig. S16 in SI), due to the plastic deformation, the peak force is decreased but the force–displacement curves largely overlap after cycling, indicating stable mechanical performance. Even with plastic deformation occurring during the folding and unfolding of monostable GO Kresling, the unloading curve approaches the origin with only a ~1 mm offset in displacement, which explains why no significant differences were observed in the macroscopic geometry of the GO origami after drying.

Through different topological designs, the humidity responsiveness of GO can be translated into distinct functions in origami structures, *i.e.*, real-time indication of device state and memory retention. This achievement shows how metamaterial engineering can enable actuations and functionalities that go beyond conventional GO humidity responsive motions and the resulting functions, which are typically limited to simple bending or twisting.

Conclusions

This study showcases macroscopic and deployable GO origamis with topology-programmed humidity-driven actuations beyond conventional bending and twisting motions. The GO origamis are fabricated using flexible GO papers, which are prepared through evaporation of Ca-containing GO suspensions on wet cellulose substrates.

Water molecule intercalation between the GO flakes during evaporation-induced paper self-assembly increases the paper tensile failure strain and reduces its stiffness. This enables the preparation of deployable macroscopic origamis with anisotropic mechanical properties or coupled compression-twisting deformations. Exploiting GO hygroscopicity and its interlayer expansion as a function of water content, the origamis can be designed with geometries that enable folding and unfolding as a function of environmental humidity. As an example, we show this can be exploited in devices that light up as a function of environmental humidity or that store a memory of high past humidity condition depending on the configuration of a set of GO-based origamis, setting the stage for the tantalizing prospect of GO-origami enabled digital computing.[88]

The methods discussed here could be used to fabricate a wide range of graphene-based topological structures thanks to the wide design space of architected origamis. Integrating magnetic, light-responsive, or piezoelectric materials into GO paper could lead to the development of multi-responsive and multifunctional actuators.[89] This versatility positions GO-based origamis as promising candidates for developing next-generation responsive devices and multifunctional soft robots.

Author contributions

Y. C. and J. C. performed the experiments, analyzed the data and wrote the paper draft. J. C. and A. S. performed the computational studies. Y. C., J. C., A.H. A. and M. C. conceptualized the research. The research was conducted under the direction and supervision of A. H. A and M. C. All authors contributed to the review and editing of the manuscript.

Conflicts of interest

There are no conflicts to declare.

Data availability

The data supporting this article have been included as part of the supplementary information (SI). Supplementary information is available. See DOI: **https://doi.org/10.1039/d5mh01681a**.

Acknowledgements

M. Cerruti and A. H. Akbarzadeh acknowledge financial support by New Frontiers in Research Fund (NFRFE-2022-00507). A. H. Akbarzadeh acknowledges the financial support of the Canada Research Chairs program in Programmable Multifunctional Metamaterials. M. Cerruti and A. H. Akbarzadeh also acknowledge funding from the Natural Sciences and Engineering Research Council of Canada through NSERC Discovery Grants (MC: RGPIN-2018-05608 and RGPIN-2024-05391; AHA: RGPIN-2022-04493, respectively) and the Canada Foundation for Innovation (CFI) through John R. Evans Leaders Fund. Y. Chen and J. Cai acknowledge the financial support provided by McGill University and by Quebec Research Fund Nature and Technologies (FRQNT) doctoral awards (B2X). J. Cai also acknowledges the financial support provided by the China Scholarship Council (File No. 201909370077). The support of Quebec Centre for Advanced Materials and McGill Institute for Advanced Materials are acknowledged. This research was enabled by support provided by Calcul Québec and Compute Canada.

References

1 K. S. Novoselov, A. K. Geim, S. V. Morozov, D. Jiang, Y. Zhang, S. V. Dubonos, I. V. Grigorieva and A. A. Firsov, *Science*, 2004, **306**, 666–669.
2 K. S. Novoselov, D. Jiang, F. Schedin, T. J. Booth, V. V. Khotkevich, S. V. Morozov and A. K. Geim, *Proc. Natl. Acad. Sci. U. S. A.*, 2005, **102**, 10451–10453.
3 Y. Chen, T. Szkopek and M. Cerruti, *Mater. Horiz.*, 2023, **10**, 2638–2648.
4 K. Hu, X. Xie, T. Szkopek and M. Cerruti, *Chem. Mater.*, 2016, **28**, 1756–1768.
5 S. Liu, K. Hu, M. Cerruti and F. Barthelat, *Carbon*, 2020, **158**, 426–434.
6 Y. Chen, X. Su, D. Esmail, E. Buck, S. D. Tran, T. Szkopek and M. Cerruti, *Carbon*, 2022, **189**, 186–198.
7 G. Capilli, Y. Chen, T. Szkopek and M. Cerruti, *ACS Nano*, 2022, **16**, 12488–12499.
8 J.-J. Shao, W. Lv and Q.-H. Yang, *Adv. Mater.*, 2014, **26**, 5586–5612.
9 J. Shi, H. Mofatteh, A. Mirabolghasemi, G. Desharnais and A. Akbarzadeh, *Adv. Mater.*, 2021, **33**, 2102423.
10 B. Shahryari, H. Mofatteh, A. Sargazi, A. Mirabolghasemi, D. Meger and A. Akbarzadeh, *Adv. Funct. Mater.*, 2024, 2407651.
11 M. C. Fernandes, J. Aizenberg, J. C. Weaver and K. Bertoldi, *Nat. Mater.*, 2021, **20**, 237–241.
12 Y. Ling, X. Zhuang, Z. Xu, Y. Xie, X. Zhu, Y. Xu, B. Sun, J. Lin, Y. Zhang and Z. Yan, *ACS Nano*, 2018, **12**, 12456–12463.
13 H. Fang, S.-C. A. Chu, Y. Xia and K.-W. Wang, *Adv. Mater.*, 2018, **30**, 1706311.
14 K. Liu, P. P. Pratapa, D. Misseroni, T. Tachi and G. H. Paulino, *Adv. Mater.*, 2022, **34**, 2107998.
15 S. Wu, T. Zhao, Y. Zhu and G. H. Paulino, *Proc. Natl. Acad. Sci. U. S. A.*, 2024, **121**, e2322625121.
16 J. A. Faber, A. F. Arrieta and A. R. Studart, *Science*, 2018, **359**, 1386–1391.
17 D. Melancon, B. Gorissen, C. J. García-Mora, C. Hoberman and K. Bertoldi, *Nature*, 2021, **592**, 545–550.
18 S. Janbaz, R. Hedayati and A. A. Zadpoor, *Mater. Horiz.*, 2016, **3**, 536–547.
19 H. Yao, X. Zhao, K. Shi, W. Sun and S. Mi, *Mater. Horiz.*, 2024, **11**, 4689–4704.
20 T. Chen, O. R. Bilal, R. Lang, C. Daraio and K. Shea, *Phys. Rev. Appl.*, 2019, **11**, 064069.
21 L. S. Novelino, Q. Ze, S. Wu, G. H. Paulino and R. Zhao, *Proc. Natl. Acad. Sci. U. S. A.*, 2020, **117**, 24096–24101.
22 R. Wang, Y. Zhang, W. Lu, B. Wu, S. Wei, S. Wu, W. Wang and T. Chen, *Angew. Chem., Int. Ed.*, 2023, **62**, e202300417.
23 M. Z. Miskin, K. J. Dorsey, B. Bircan, Y. Han, D. A. Muller, P. L. McEuen and I. Cohen, *Proc. Natl. Acad. Sci. U. S. A.*, 2018, **115**, 466–470.
24 H. Kim, J. A. Lee, C. P. Ambulo, H. B. Lee, S. H. Kim, V. V. Naik, C. S. Haines, A. E. Aliev, R. Ovalle-Robles, R. H. Baughman and T. H. Ware, *Adv. Funct. Mater.*, 2019, **29**, 1905063.
25 W. Kim, J. Byun, J.-K. Kim, W.-Y. Choi, K. Jakobsen, J. Jakobsen, D.-Y. Lee and K.-J. Cho, *Sci. Robot.*, 2019, **4**, eaay3493.
26 D. Joung, A. Nemilentsau, K. Agarwal, C. Dai, C. Liu, Q. Su, J. Li, T. Low, S. J. Koester and J.-H. Cho, *Nano Lett.*, 2017, **17**, 1987–1994.
27 W. Xu, Z. Qin, C.-T. Chen, H. R. Kwag, Q. Ma, A. Sarkar, M. J. Buehler and D. H. Gracias, *Sci. Adv.*, 2017, **3**, e1701084.
28 T. Deng, C. Yoon, Q. Jin, M. Li, Z. Liu and D. H. Gracias, *Appl. Phys. Lett.*, 2015, **106**, 203108.
29 F. Guo, Y. Wang, Y. Jiang, Z. Li, Z. Xu, X. Zhao, T. Guo, W. Jiang and C. Gao, *Adv. Mater.*, 2021, **33**, 2008116.
30 L. Peng, Z. Xu, Z. Liu, Y. Guo, P. Li and C. Gao, *Adv. Mater.*, 2017, **29**, 1700589.
31 Y. Guo, C. Dun, J. Xu, J. Mu, P. Li, L. Gu, C. Hou, C. A. Hewitt, Q. Zhang, Y. Li, D. L. Carroll and H. Wang, *Small*, 2017, **13**, 1702645.
32 D.-D. Han, Y.-L. Zhang, Y. Liu, Y.-Q. Liu, H.-B. Jiang, B. Han, X.-Y. Fu, H. Ding, H.-L. Xu and H.-B. Sun, *Adv. Funct. Mater.*, 2015, **25**, 4548–4557.
33 Y. Chen, M. Qu, C. Liu, S. Li, X. Wang, D. Gong, P. Tang and Y. Bin, *Chem. Eng. J.*, 2025, **515**, 163927.

34 M. Weng, J. Zhou, P. Zhou, R. Shang, M. You, G. Shen and H. Chen, *Adv. Sci.*, 2024, **11**, 2309846.
35 L. Chen, M. Weng, P. Zhou, L. Zhang, Z. Huang and W. Zhang, *Nanoscale*, 2017, **9**, 9825–9833.
36 Y.-L. Zhang, J.-N. Ma, S. Liu, D.-D. Han, Y.-Q. Liu, Z.-D. Chen, J.-W. Mao and H.-B. Sun, *Nano Energy*, 2020, **68**, 104302.
37 M. Liu, Y. Yao, X. He, Z. Li, Y. Liu, H. Tao, Z. Li, Y. Zhang, L. Wang, H. Zhang and X. Qin, *Nano Lett.*, 2025, **25**, 9318–9326.
38 H. Cheng, F. Zhao, J. Xue, G. Shi, L. Jiang and L. Qu, *ACS Nano*, 2016, **10**, 9529–9535.
39 J. Mu, C. Hou, H. Wang, Y. Li, Q. Zhang and M. Zhu, *Sci. Adv.*, 2015, **1**, e1500533.
40 B. Treml, A. Gillman, P. Buskohl and R. Vaia, *Proc. Natl. Acad. Sci. U. S. A.*, 2018, **115**, 6916–6921.
41 Y. Ge, R. Cao, S. Ye, Z. Chen, Z. Zhu, Y. Tu, D. Ge and X. Yang, *Chem. Commun.*, 2018, **54**, 3126–3129.
42 Y.-Q. Liu, Z.-D. Chen, D.-D. Han, J.-W. Mao, J.-N. Ma, Y.-L. Zhang and H.-B. Sun, *Adv. Sci.*, 2021, **8**, 2002464.
43 X. Zhang, C. Song, H. Nong, K. Xu, X. Wu, W. Zhong, M. Xing and L. Wang, *Adv. Funct. Mater.*, 2023, **33**, 2300866.
44 W. Yan, Y. Feng, J. Song, Z. Hong, K. Cui, A. C. Brannan, J. Sun, J. Tan and X. Song, *Carbon*, 2025, **231**, 119734.
45 Y. Dong, J. Wang, X. Guo, S. Yang, M. O. Ozen, P. Chen, X. Liu, W. Du, F. Xiao, U. Demirci and B.-F. Liu, *Nat. Commun.*, 2019, **10**, 4087.
46 D. A. Dikin, S. Stankovich, E. J. Zimney, R. D. Piner, G. H. B. Dommett, G. Evmenenko, S. T. Nguyen and R. S. Ruoff, *Nature*, 2007, **448**, 457–460.
47 S. Ye, B. Chen and J. Feng, *Sci. Rep.*, 2015, **5**, 13102.
48 T. Gong, D. V. Lam, R. Liu, S. Won, Y. Hwangbo, S. Kwon, J. Kim, K. Sun, J.-H. Kim, S.-M. Lee and C. Lee, *Adv. Funct. Mater.*, 2015, **25**, 3756–3763.
49 R. Cruz-Silva, A. Morelos-Gomez, H. Kim, H. Jang, F. Tristan, S. Vega-Diaz, L. P. Rajukumar, A. L. Elías, N. Perea-Lopez, J. Suhr, M. Endo and M. Terrones, *ACS Nano*, 2014, **8**, 5959–5967.
50 W. Cui, M. Li, J. Liu, B. Wang, C. Zhang, L. Jiang and Q. Cheng, *ACS Nano*, 2014, **8**, 9511–9517.
51 K. W. Putz, O. C. Compton, M. J. Palmeri, S. T. Nguyen and L. C. Brinson, *Adv. Funct. Mater.*, 2010, **20**, 3322–3329.
52 S. Park, K.-S. Lee, G. Bozoklu, W. Cai, S. T. Nguyen and R. S. Ruoff, *ACS Nano*, 2008, **2**, 572–578.
53 Y. Gao, L.-Q. Liu, S.-Z. Zu, K. Peng, D. Zhou, B.-H. Han and Z. Zhang, *ACS Nano*, 2011, **5**, 2134–2141.
54 Z. An, O. C. Compton, K. W. Putz, L. C. Brinson and S. T. Nguyen, *Adv. Mater.*, 2011, **23**, 3842–3846.
55 Q. Cheng, M. Wu, M. Li, L. Jiang and Z. Tang, *Angew. Chem.*, 2013, **125**, 3838–3843.
56 A. Satti, P. Larpent and Y. Gunko, *Carbon*, 2010, **48**, 3376–3381.
57 M. Zhang, L. Huang, J. Chen, C. Li and G. Shi, *Adv. Mater.*, 2014, **26**, 7588–7592.
58 Z. Liu, Z. Li, Z. Xu, Z. Xia, X. Hu, L. Kou, L. Peng, Y. Wei and C. Gao, *Chem. Mater.*, 2014, **26**, 6786–6795.
59 L. Huang, C. Li, W. Yuan and G. Shi, *Nanoscale*, 2013, **5**, 3780–3786.
60 X.-B. Lv, R. Xie, J.-Y. Ji, Z. Liu, X.-Y. Wen, L.-Y. Liu, J.-Q. Hu, X.-J. Ju, W. Wang and L.-Y. Chu, *ACS Appl. Mater. Interfaces*, 2020, **12**, 56269–56280.
61 C. Chen, Q.-H. Yang, Y. Yang, W. Lv, Y. Wen, P.-X. Hou, M. Wang and H.-M. Cheng, *Adv. Mater.*, 2009, **21**, 3007–3011.
62 X. Ye, Q. Zhou, C. Jia, Z. Tang, Y. Zhu and Z. Wan, *Carbon*, 2017, **114**, 424–434.
63 D. Kang, Z. Cai, Q. Jin and H. Zhang, *Carbon*, 2015, **91**, 445–457.
64 C.-N. Yeh, K. Raidongia, J. Shao, Q.-H. Yang and J. Huang, *Nat. Chem.*, 2015, **7**, 166–170.
65 S. Park, D. A. Dikin, S. T. Nguyen and R. S. Ruoff, *J. Phys. Chem. C*, 2009, **113**, 15801–15804.
66 Y.-Q. Li, T. Yu, T.-Y. Yang, L.-X. Zheng and K. Liao, *Adv. Mater.*, 2012, **24**, 3426–3431.
67 J. Y. Chong, B. Wang and K. Li, *Chem. Commun.*, 2018, **54**, 2554–2557.
68 X. Lin, X. Shen, Q. Zheng, N. Yousefi, L. Ye, Y.-W. Mai and J.-K. Kim, *ACS Nano*, 2012, **6**, 10708–10719.
69 S. Zheng, Q. Tu, J. J. Urban, S. Li and B. Mi, *ACS Nano*, 2017, **11**, 6440–6450.
70 K. W. Putz, O. C. Compton, C. Segar, Z. An, S. T. Nguyen and L. C. Brinson, *ACS Nano*, 2011, **5**, 6601–6609.
71 K. Krishnamoorthy, M. Veerapandian, K. Yun and S.-J. Kim, *Carbon*, 2013, **53**, 38–49.
72 Z. Y. Wei, Z. V. Guo, L. Dudte, H. Y. Liang and L. Mahadevan, *Phys. Rev. Lett.*, 2013, **110**, 215501.
73 E. T. Filipov, T. Tachi and G. H. Paulino, *Proc. Natl. Acad. Sci. U. S. A.*, 2015, **112**, 12321–12326.
74 Z. Lin, L. S. Novelino, H. Wei, N. A. Alderete, G. H. Paulino, H. D. Espinosa and S. Krishnaswamy, *Small*, 2020, **16**, 2002229.
75 J. Zhang, D. Karagiozova, Z. You, Y. Chen and G. Lu, *Int. J. Mech. Sci.*, 2019, **153–154**, 194–207.
76 K. Liu and G. H. Paulino, *Proc. R. Soc. Math. Phys. Eng. Sci.*, 2017, **473**, 20170348.
77 E. Boatti, N. Vasios and K. Bertoldi, *Adv. Mater.*, 2017, **29**, 1700360.
78 R. J. Lang, *Twists, Tilings, and Tessellations: Mathematical Methods for Geometric Origami*, ed. A. K. Peters, CRC Press, New York, 2017.
79 S. Borini, R. White, D. Wei, M. Astley, S. Haque, E. Spigone, N. Harris, J. Kivioja and T. Ryhänen, *ACS Nano*, 2013, **7**, 11166–11173.
80 A. Iakunkov and A. V. Talyzin, *Nanoscale*, 2020, **12**, 21060–21093.
81 J. Cai, B. Shahryari and A. Akbarzadeh, *MRS Bull.*, 2024, **49**, 38–48.
82 J. Cai, E. Estakhrianhaghighi and A. Akbarzadeh, *Carbon*, 2022, **191**, 610–624.
83 M. Schenk and S. D. Guest, *Proc. Natl. Acad. Sci. U. S. A.*, 2013, **110**, 3276–3281.
84 F. Guo, F. Kim, T. H. Han, V. B. Shenoy, J. Huang and R. H. Hurt, *ACS Nano*, 2011, **5**, 8019–8025.

85 J. Cai, B. Yang and A. Akbarzadeh, *ACS Nano*, 2024, **18**, 894–908.
86 D. T. Ho, H. S. Park, S. Y. Kim and U. Schwingenschlögl, *ACS Nano*, 2020, **14**, 8969–8974.
87 S. Zhu and T. Li, *ACS Nano*, 2014, **8**, 2864–2872.
88 H. Mofatteh, B. Shahryari, A. Mirabolghasemi, A. Seyedkanani, R. Shirzadkhani, G. Desharnais and A. Akbarzadeh, *Adv. Sci.*, 2022, **9**, 2202883.
89 J. Cai, Y. Chen, A. Seyedkanani, G. Shen, M. Cerruti and A. Akbarzadeh, *Adv. Sci.*, 2025, 202514597.